Role of B19' martensite deformation in stabilizing two-way shape memory behavior in NiTi

O. Benafan, S. A. Padula, R. D. Noebe, et al.

View Online

Export Citation

ARTICLES YOU MAY BE INTERESTED IN

Effect of Low-Temperature Phase Changes on the Mechanical Properties of Alloys near Composition TiNi
Journal of Applied Physics **34**, 1475 (1963); https://doi.org/10.1063/1.1729603

Structural transformations in NiTi shape memory alloy nanowires
Journal of Applied Physics **115**, 194307 (2014); https://doi.org/10.1063/1.4876715

Texture evolution during nitinol martensite detwinning and phase transformation
Applied Physics Letters **103**, 241909 (2013); https://doi.org/10.1063/1.4846495

Role of B19′ martensite deformation in stabilizing two-way shape memory behavior in NiTi

O. Benafan,[1,2,a)] S. A. Padula II,[2] R. D. Noebe,[2] T. A. Sisneros,[3] and R. Vaidyanathan[1]

[1]*Advanced Materials Processing and Analysis Center (AMPAC), Mechanical, Materials, and Aerospace Engineering Department, University of Central Florida, Orlando, Florida 32816, USA*
[2]*NASA Glenn Research Center, Structures and Materials Division, Cleveland, Ohio 44135, USA*
[3]*Los Alamos National Laboratory, Los Alamos, New Mexico 87545, USA*

Deformation of a B19′ martensitic, polycrystalline $Ni_{49.9}Ti_{50.1}$ (at. %) shape memory alloy and its influence on the magnitude and stability of the ensuing two-way shape memory effect (TWSME) was investigated by combined *ex situ* mechanical experimentation and *in situ* neutron diffraction measurements at stress and temperature. The microstructural changes (texture, lattice strains, and phase fractions) during room-temperature deformation and subsequent thermal cycling were captured and compared to the bulk macroscopic response of the alloy. With increasing uniaxial strain, it was observed that B19′ martensite deformed by reorientation and detwinning with preferred selection of the $(\bar{1}50)_M$ and $(010)_M$ variants, $(20\bar{1})_{B19'}$ deformation twinning, and dislocation activity. These mechanisms were indicated by changes in bulk texture from the neutron diffraction measurements. Partial reversibility of the reoriented variants and deformation twins was also captured upon load removal and thermal cycling, which after isothermal deformation to strains between 6% and 22% resulted in a strong TWSME. Consequently, TWSME functional parameters including TWSME strain, strain reduction, and transformation temperatures were characterized and it was found that prior martensite deformation to 14% strain provided the optimum condition for the TWSME, resulting in a stable two-way shape memory strain of 2.2%. Thus, isothermal deformation of martensite was found to be a quick and efficient method for creating a strong and stable TWSME in $Ni_{49.9}Ti_{50.1}$. © *2012 American Institute of Physics*. [http://dx.doi.org/10.1063/1.4764313]

I. INTRODUCTION

Near-equiatomic NiTi shape memory alloys (SMAs) undergo a reversible martensitic phase transformation between a cubic (B2) austenite phase and a monoclinic (B19′) martensite phase. This first-order phase transformation gives SMAs their unique shape recovery capabilities, exemplified by two behaviors: the shape memory effect (temperature-induced phase transformation) and superelasticity (stress-induced phase transformation). Both behaviors have been widely exploited in a range of applications in response to aerospace, biomedical, and industrial needs, amongst others.[1] NiTi SMAs can produce work (energy densities exceeding 10^7 J/m^3),[2] which allows them to be employed as solid-state actuators. Typically when used in such applications, the SMA elements remember the original austenitic shape and are used in conjunction with a biasing force to complete the actuation cycle. This is known as biased shape memory or one-way shape memory behavior. It is also possible for these alloys to change and remember shapes on both heating and cooling without an external biasing force, a behavior known as the two-way shape memory effect (TWSME). TWSME is not an inherent behavior of SMAs but can be obtained after specific thermomechanical training procedures.

Extensive research exists concerning the various methods used for inducing the TWSME.[3] Some of these training procedures consist of constant load thermal cycling (e.g., in NiTi,[4–7] NiTiPd,[7,8] CuZnAl,[9,10] and TiNiNb[11]), martensite deformation and free/constrained recovery (e.g., in tension,[12–14] compression,[15] and bending[16–19]), deformation cycling of austenite to promote the stress-induced martensitic transformation,[20–22] or precipitation during constrained aging.[23–26] The principle behind all these training methods involves the formation of internal stress fields that induce the same martensite variants during transformation as were generated during training, but without the need for external stress. These stresses can be created by mechanisms such as dislocation arrays generated during thermomechanical training,[10,20] stabilized stress-induced martensite,[22] retained martensite,[14,20] symmetry and point defects,[27] or aligned coherent precipitates.[23] The associated internal stresses that are developed during these training procedures dictate the stability and efficiency of the TWSME. Thus, understanding the role of the adopted training schemes is essential in optimizing the performance of the ensuing two-way shape memory response.

Martensite deformation is probably the simplest but least understood training scheme. B19′ martensite deformation proceeds through several mechanisms that operate over distinct strain ranges. Fig. 1 is a representative stress-strain curve for martensitic NiTi, which for discussion purposes is divided into four main regions. Region I is the initial

---

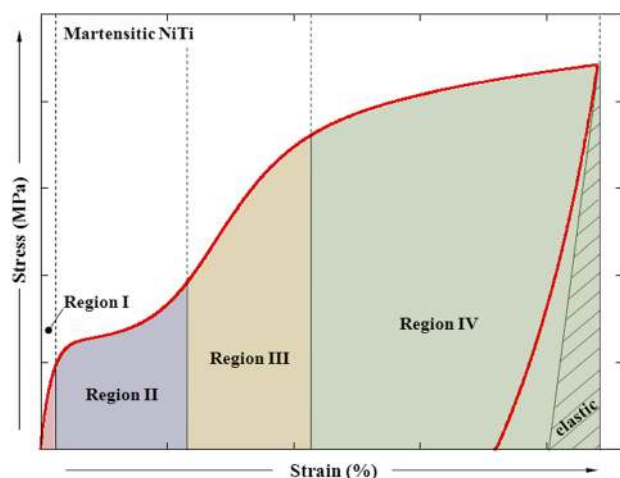a)Author to whom correspondence should be addressed. Electronic mail: othmane.benafan@nasa.gov.

FIG. 1. Representative stress-strain response of martensitic NiTi showing the four distinct deformation regimes.

macroscopic tensile response up to ~1% strain, which is attributed to the elastic deformation of the self-accommodated B19′ martensite coupled with early onset of variant reorientation and detwinning.[28] These latter processes are responsible for the non-linearity observed in the initial loading response of NiTi and the often deflated values of modulus reported from mechanical test data. With increasing strain (region II), a broad stress plateau is obtained where the deformation is mainly dominated by variant reorientation and detwinning of the initial [011] type II and (1$\bar{1}$1) type I twinning modes.[29–31] In this same region, it has been reported that dislocation networks form in both the martensite twin plates[32] and in the junction plane areas[33] to accommodate the strain mismatch during variant reorientation. Further straining results in region III of rapid strain hardening, which is attributed to further reorientation and detwinning, the operation of new (20$\bar{1}$) and (100) deformation twins[30,31,34] and plasticity. Finally, region IV, with a characteristic low work hardening rate, is due to further nucleation and growth of (100) and (20$\bar{1}$) deformation twin systems, possible formation of new (113) twins,[30,31] and dislocation generation.[13,30]

Training via martensite deformation has been shown to be effective in inducing the TWSME.[13] Compared to other methods, training by martensite deformation is relatively easy and quick, requiring little more than a onetime deformation of the material as opposed to aging under some type of constraint or performing multiple thermomechanical cycles. While theories have been proposed to explain this training route, no experimental studies have examined the micromechanical and microstructural changes associated with the martensite deformation that is responsible for development of the TWSME (e.g., texture evolution, internal strain fields, and phase volume fractions). In addition, the underlying martensite deformation mechanisms discussed above have not been linked to optimization of the TWSME. One way of investigating these microstructural parameters is by *in situ* neutron diffraction at stress and temperature. Neutrons are uniquely suited to study the average microstructural response of bulk polycrystalline samples due to

the deep penetration, large sampling volume, and elimination of free-surface effects. Therefore, use of *in situ* neutron diffraction coupled with *ex situ* macroscopic testing can provide additional insights into the B19′ deformation mechanisms previously discussed and the ensuing TWSME.

Thus, the aim of this work was to investigate the role of martensite deformation on the stability and efficacy of the TWSME by carrying out *in situ* neutron diffraction measurements during isothermal loading and thermomechanical cycling. TWSME functional parameters and degradation (or lack thereof) were also measured from *ex situ* macroscopic experiments and correlated with the microstructural observations.

II. EXPERIMENTAL TECHNIQUES

The material used in this study was a binary NiTi alloy with nominal composition of $Ni_{49.9}Ti_{50.1}$ (at. %) produced by Special Metals, New Hartford, New York (now SAES Smart Materials). Cylindrical, dog-bone tensile specimens, 5.08 mm in diameter and 15.24 mm in gauge length, were machined from a hot-rolled and hot-straightened 10 mm diameter rod. Various physical and thermomechanical properties of this alloy are available in the literature.[7,28,35–38] Prior to testing, two no-load thermal cycles between room temperature and 200 °C at a rate of 20 °C/min were performed on the as-machined samples to relieve any residual stresses resulting from the machining operation. Stress-free transformation temperatures: martensite start (M_s), martensite finish (M_f), austenite start (A_s), and austenite finish (A_f) were measured from the second mechanical no-load thermal cycle using the intercept method and were found to be 71, 55, 92, and 105 ± 2 °C, respectively. From differential scanning calorimetry (DSC) measurements, no intermediate R-phase or multistage transformation was observed in this alloy.

Ex situ thermomechanical tests were performed on an 810 MTS servohydraulic load frame equipped with an MTS FlexTest SE digital controller, a Eurotherm 3504 temperature controller, an Ameritherm NovaStar 7.5 kW induction heater, a set of 646 water cooled hydraulic collet grips, a 22 kN/5 kip load cell, and a high-temperature, 12.7 mm gauge length extensometer. The *ex situ* experiments consisted of isothermal loading and unloading at room temperature followed by stress-free thermal cycling. Seven samples were strained individually in uniaxial tension to 6%, 10%, 14%, 16%, 18%, 20%, and 22% in strain control at a rate of 1×10^{-4} s^{-1} (Fig. 2). The maximum strain imparted to each sample was selected specifically to study the deformation response of martensite in different regions of Fig. 1. The microstructural response of NiTi during the initial loading up to 6% strain has been thoroughly investigated in Ref. 28 and hence omitted in this study. After straining each sample to a predetermined value, it was then unloaded to 0 MPa and thermally cycled 10-times through the phase transformation between room temperature and 200 °C using a heating rate of 20 °C/min (while holding the stress constant at 0 MPa).

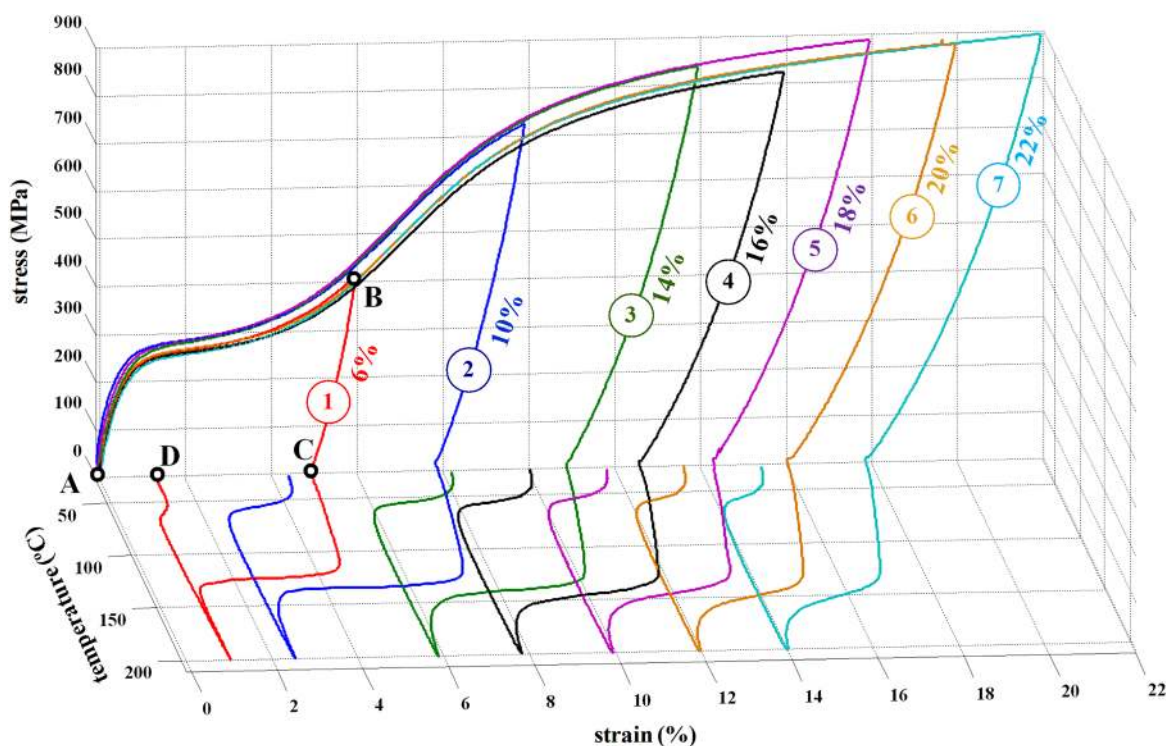*In situ* neutron diffraction experiments were performed in "time-of-flight" mode using the spectrometer for MAterials

FIG. 2. Tensile stress-strain-temperature responses of seven $Ni_{49.9}Ti_{50.1}$ samples deformed at room temperature to strains between 6% and 22%, unloaded to zero stress, and thermally cycled to 200 °C and back to room temperature.

Research at Temperature and Stress (SMARTS) at the pulsed neutron source at Los Alamos National Laboratory (LANL). A detailed description of the experimental instrument can be found elsewhere.[39] In SMARTS, the samples were mechanically loaded in tension while simultaneously acquiring neutron data with diffraction vectors parallel ($Q_{\parallel}$, −90°) and perpendicular ($Q_{\perp}$, +90°) to the loading axis (loading axis oriented at 45° relative to the incident beam). Similar to the *ex situ* experiments, five samples were individually strained *in situ* to 6%, 10%, 14%, 18%, and 22%, unloaded to 0 MPa, heated to 200 °C, and cooled to room temperature using the same strain and heating rates listed above. Neutron diffraction spectra were collected at each step, i.e., at room temperature in the initial no-load condition, at the applied strain achieved after tensile loading, and after unloading at 0 MPa, during heating at 200 °C, and again at room temperature after the cooling cycle. At each condition, neutron spectra were acquired for 30 min for adequate statistical quality.

The Rietveld refinement technique[40] implemented in the General Structure Analysis System (GSAS) code[41,42] was used to analyze the neutron diffraction spectra. A generalized spherical harmonic description[42] was used in the code to capture the texture evolution during loading and/or heating. In this work, texture is represented using inverse pole figures (IPFs), which describe the distribution of specific macroscopic directions, particularly, the loading axis, in the coordinate systems of the individual diffracting units that compose polycrystalline NiTi. A single peak fitting method was also used to compute individual *hkl* lattice strains from planes perpendicular to the loading direction using the change in the interplanar spacing as described elsewhere.[37]

III. RESULTS AND DISCUSSION

A. B19′ martensite deformation

The tensile stress-strain-temperature response of the $Ni_{49.9}Ti_{50.1}$ alloy is shown in Fig. 2 for 7 samples deformed at room temperature to strains between 6% and 22%, unloading to zero stress, followed by thermal cycling. For clarity, only the first heating cycle is shown, though each sample was thermally cycled 10-times between room temperature and 200 °C. The first thermal cycle, included in Fig. 2, will be referred to as the transient response in subsequent discussion.

The effect of martensite deformation on the subsequent strain recovery of the $Ni_{49.9}Ti_{50.1}$ alloy is shown in Fig. 3. The amount of springback after unloading (from the applied strain to 0 MPa (B→C)) and the amount of strain recovery after the first thermal cycle at 0 MPa (C→D) are shown in Fig. 3(a). The letters A-D refer to positions along the stress-strain-temperature curves indicated in Fig. 2. The data indicate that the strain recovery due to unloading (B to C) increased with increasing applied strain but was larger than anticipated based solely on elastic recovery. The recovered strain due to the first thermal cycle (C to D) appeared as a step function, decreasing to a lower level between 10% and 14% applied strain, as region IV of Fig. 1 is reached.

However, if the two strain recovery mechanisms are combined (B to D) the total strain recovery increases with increasing applied strain (Fig. 3(b)). The permanent component of the strains (D to A) also increased with applied strain, increasing in a nearly linear fashion. These observations are qualitatively consistent with a previous study.[13] The maximum total recoverable strain was 6.6% for sample 7, which
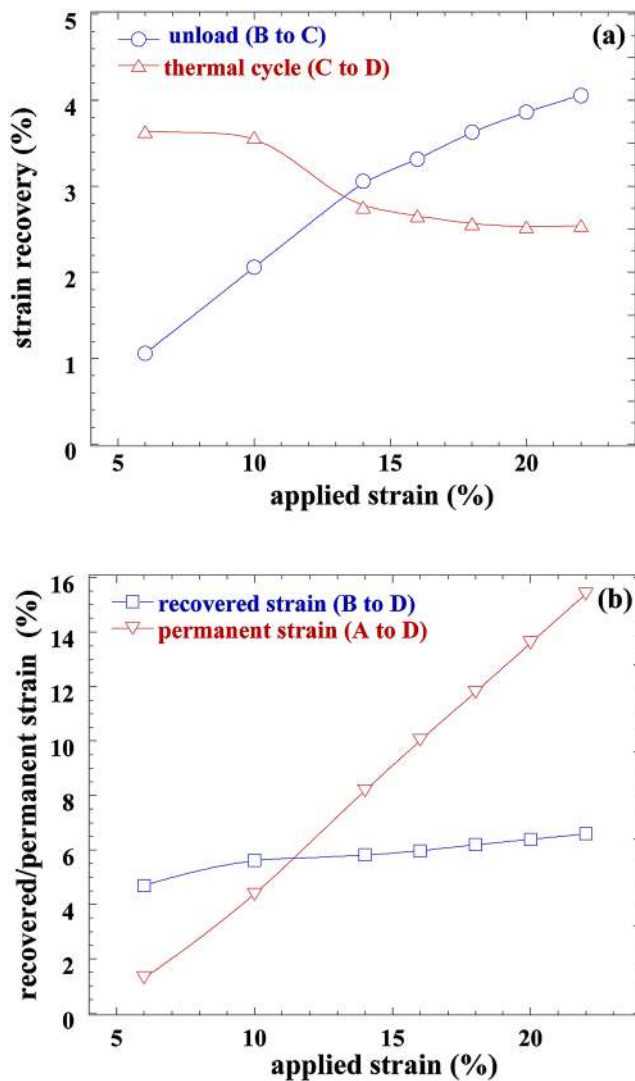
FIG. 3. Recovered and permanent strains through various regions of the stress-strain-temperature curves for $Ni_{49.9}Ti_{50.1}$ shown in Fig. 2. (a) Recovered strains after unloading (from the applied strain to 0 MPa (B→C)) and after the first thermal cycle at 0 MPa (C→D). (b) Total recovered strains including unloading and thermal recovery (B to D) and total permanent strains after the first thermal cycle (D to A).

was strained to 22%. However, the maximum thermally recovered strain occurred in the sample deformed only to 6%. The permanent strains become larger than the recovered strain at about 11.5% strain, as indicated by the line crossing in Fig. 3(b), which is the beginning of region IV of Fig. 1. Overall, the linearity in both the total recovered and the permanent strains shown in Fig. 3(b) and the step function in the thermally recovered strain as a function of applied strain implies that martensite deformation from 11% to 22% is possibly dominated by the same mechanism(s).

Neutron diffraction data were collected at critical points (i.e., positions A, B, C, and D of Fig. 2) to relate the observed macroscopic behaviors to microstructural mechanism(s). Fig. 4 shows the IPFs for planes perpendicular to the loading axis in the $B19'$ martensite for samples 1(6%), 2(10%), 3(14%), 5(18%), and 7(22%). The value in parentheses after each sample number is the applied strain, in which each sample was deformed initially. The numbers at

the top left-hand corner of each IPF in Fig. 4 indicate the respective maximum and minimum densities of grains with the given pole in the loading direction in multiples of random distribution. For reference, the preferred $B19'$ variants that were selected during deformation (i.e., $(\bar{1}50)_M$, $(010)_M$, and $(230)_M$) are indicated on the very first IPF (top left-hand corner). The initial near random texture for the samples prior to testing, shown in column A of Fig. 4, corresponds to the self-accommodated variants of the martensite phase as they exist in the bulk, polycrystalline aggregate. A similar initial texture was obtained for each sample tested.

On loading to 6% strain, direct evidence of variant reorientation/detwinning is presented by the texture evolution of the preferred $(\bar{1}50)_M$ and $(010)_M$ orientations (column B of Fig. 4). The initial nucleation and growth of these variants in regions I and II along the loading direction were captured in detail in Ref. 28. As observed in Fig. 2, the 6% applied strain level resides in the initial portion of the rehardening region (region III of Fig. 1), where the intensity of the $(010)_M$ orientations was observed to saturate with increasing strain. In fact, continuous texture measurements (not shown here) revealed that the intensities at the $(\bar{1}50)_M/(010)_M$ orientations reach a maximum between 7% and 9% strain where the intensity of the $(230)_M$ orientations starts to increase.[43] This is consistent with the IPF results in column B, where by 10% strain, which is just beyond the end of region III, the intensity of the $(010)_M$ orientations is just starting to decrease and the intensity of the $(230)_M$ orientations is just starting to develop.

As the intensities of the $(\bar{1}50)_M$ and $(010)_M$ orientations reached a maximum, a new texture formed with increasing applied strain, indicated by preferred selection of the $(230)_M$ orientations as shown by the IPFs in column B of Fig. 4. This discrete reorientation of the maximum pole density from crystallites whose near $(010)_M$ plane normals were aligned with the loading axis to those whose $(230)_M$ plane normals become aligned with the loading direction starts between 6% and 10% strain and dominates the behavior at the higher strain levels. It is also observed that the intermediate area of the IPFs between the $(010)_M$ and $(230)_M$ orientations gets slightly populated during this discrete reorientation. The discrete texture shift was related to $(20\bar{1})_{B19'}$ deformation twinning, which is the plane normal that bisects the real directions of the $(010)_M$ and $(230)_M$ poles.[43]

TEM studies by Zhang *et al.*[30] indicated that $(20\bar{1})_{B19'}$ deformation twinning was found to start at about 7% strain. In addition $(100)_{B19'}$ twinning was also observed by Zhang *et al.*[30] to take place before and in conjunction with the identified $(20\bar{1})_{B19'}$ twins in regions III and IV. Consistently, these TEM results show evidence of $(20\bar{1})_{B19'}$ deformation twinning at relatively low strains (∼7%), and the bulk texture results shown in Fig. 4 indicate that this deformation mode begins to form at applied strains between 6% and 10%, which corresponds to region III of the stress-strain response for martensite. In this region, the intensity of the $(230)_M$ orientations continue to increase over the level of strains investigated. Note that the region of the IPFs between the $(010)_M$ and $(230)_M$ orientations is not completely
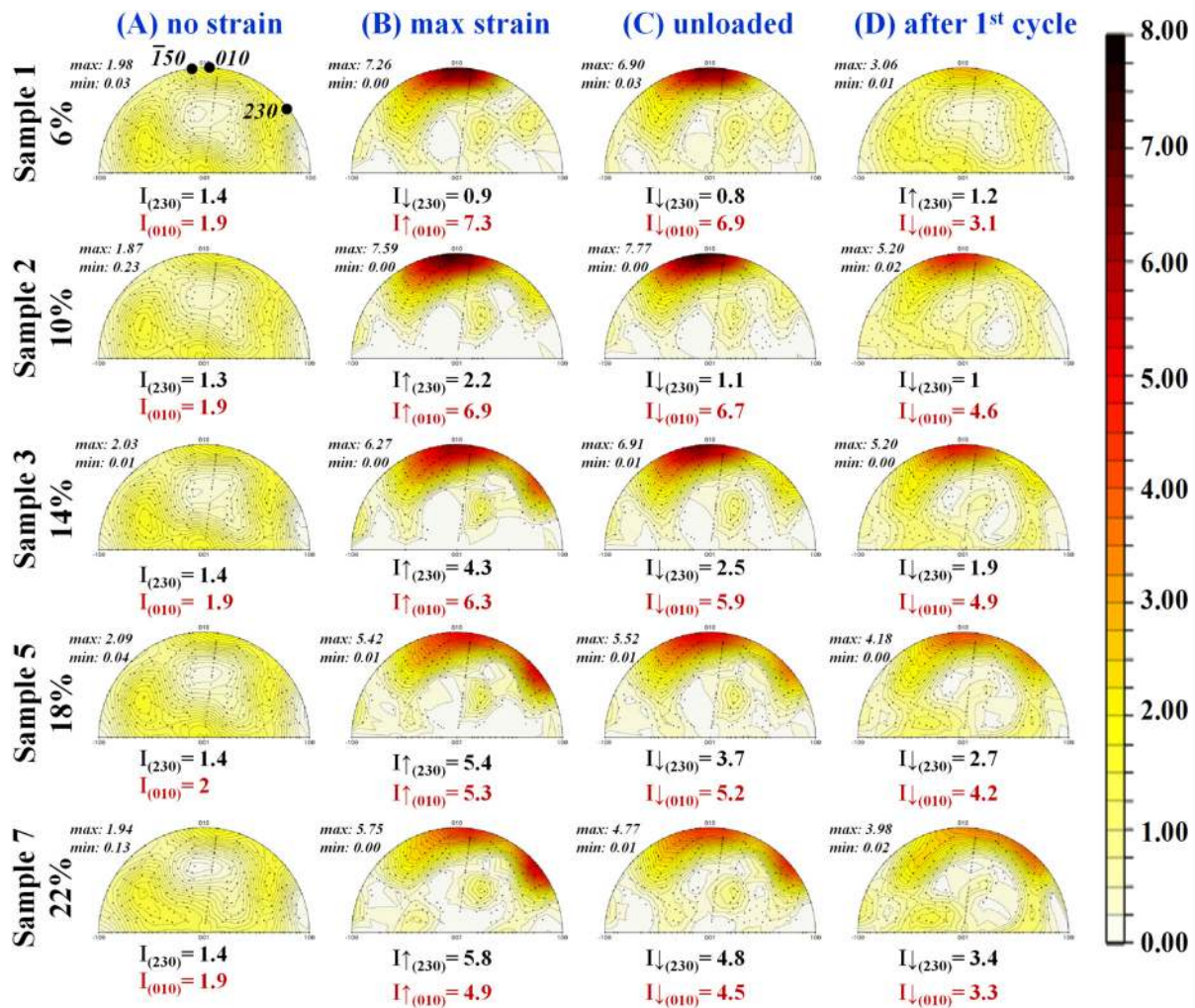
FIG. 4. Room temperature IPFs for martensitic $Ni_{49.9}Ti_{50.1}$ from diffracting planes perpendicular to the loading direction. For a given IPF, the corresponding maximum and minimum pole intensities (times random) are at the top left hand corner and the specific intensity changes for the (230) and (010) poles are indicated below each IPFs. The column letters correspond to the positions identified in Fig. 2.

unpopulated due to a gradual rotation of the maximum pole density. This is consistent with what is observed when slip mechanisms are activated, although the slip plane and direction were not identified in this work due to the difficulty in studying the dislocation structures within the martensite.

The mechanical unloading sections of the stress-strain curves shown in Fig. 2 were nonlinear in nature, which was attributed to the reverse reorientation of the martensite. This is captured by the IPFs in column C of Fig. 4 that show a decrease in the maximum pole density at the $(230)_M$ orientation and a slight decrease in the intensities of the $(\bar{1}50)_M$ and $(010)_M$ orientations after the samples were unloaded from the applied strain. Clearly, some of the $(20\bar{1})_{B19'}$ twins were partially reverted, contributing to the recovered strains during mechanical unloading (Fig. 3).

Significantly more of the $(\bar{1}50)_M$ and $(010)_M$ orientations were recovered in all samples during the first heating and cooling cycle (column D of Fig. 4). In addition, $(230)_M$ orientations were thermally recovered in samples deformed to 14%-22% strain. In samples deformed to less strain, the $(230)_M$ intensity was unaffected and very close to that of a random distribution in the samples deformed to 6% and 10%

strain in the unloaded condition following thermal cycling. This is consistent with the fact that the $(20\bar{1})_{B19'}$ twinning mode, which is presumably responsible for the $(230)_M$ texture changes, only begins to dominate at strain levels corresponding to region IV. This results in permanent strain in the martensite phase as shown in Fig. 3(b). It was also reported[30] that the $(100)_{B19'}$ twins are recoverable upon heating, which could add to the strain recovery of Fig. 3. However, the self accommodated texture of the initial martensite (column A compared to column D in Fig. 4) was not completely restored after one thermal cycle. This is due to preferential nucleation of the martensite variants favored during isothermal straining as the sample cools back to room temperature, possibly as a result of internal stresses from the $(20\bar{1})_{B19'}$ twins and dislocation activity. This preferred nucleation of selected martensite variants is responsible for the TWSME. From the presented IPFs, the large strain recovery in this $Ni_{49.9}Ti_{50.1}$ alloy is attributed to the reorientation and detwinning mechanisms (regions I and II), while the deformation twins along with dislocation generation are for the most part irreversible and lead to the permanent strains (regions III and IV). These latter mechanisms are responsible for the

70% permanent deformation in sample 7 deformed to 22% as shown in Fig. 3(b) and the permanent strain in the other samples.

The no-load, transient strain-temperature responses of the first heating and cooling cycle after room-temperature deformation are shown in Fig. 5(a). These responses were offset to a common starting point for easier comparison between samples as shown in Fig. 5(b). On heating, strains were already recovered (negative slopes) before reaching the transition temperatures where the material starts transforming to austenite. The negative slopes for the heating curves
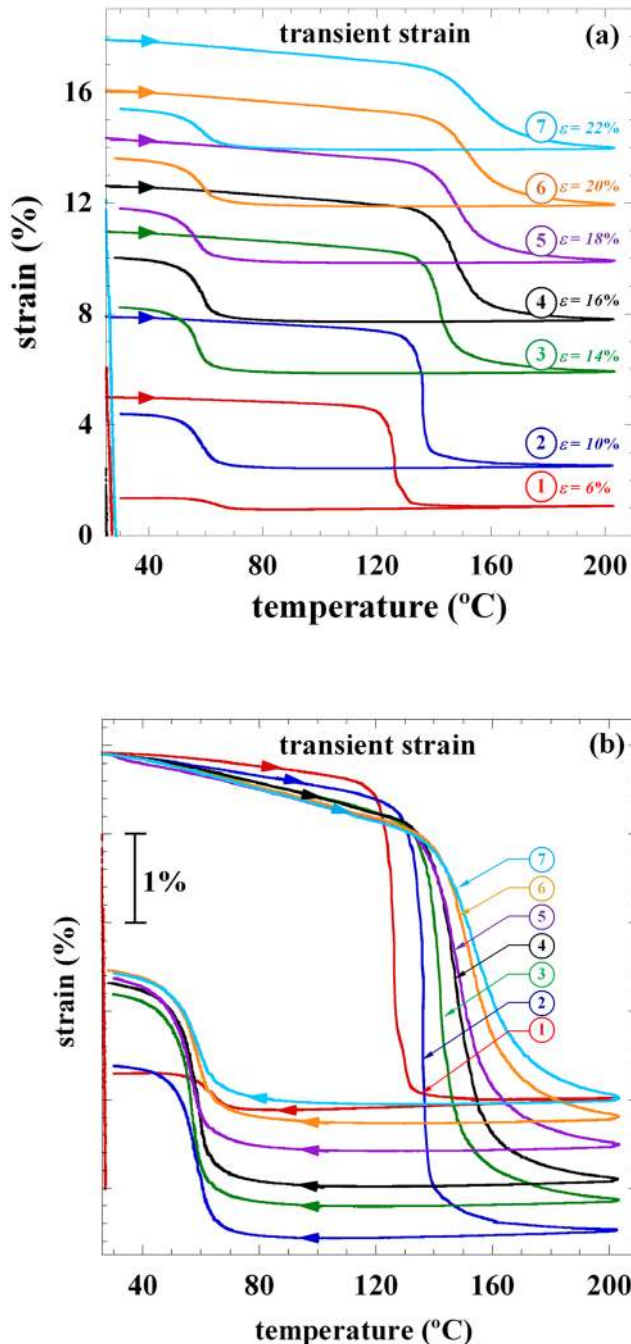

FIG. 5. Transient strain-temperature responses for the very first thermal cycle after load removal. (a) Responses in the absolute scale, (b) responses shifted to a common point. Samples 1 through 7 correspond to the samples identified in Fig. 2.

or strain recovery could possibly be attributed to at least three mechanisms: (i) negative thermal expansion, (ii) reverse reorientation of the martensite, and (iii) a change in the material compliance. It was recently shown that due to the anisotropy in the monoclinic structure, certain martensite variants exhibit a negative thermal expansion.[37] However, all the variants that formed along the loading direction for this material had a positive CTE and therefore cannot contribute to the observed transient response.

Eliminating (i) above leads to consideration of the latter two mechanisms. Additional reverse reorientation with the application of temperature occurs as some variants and deformation twins partially rearrange in the martensite matrix prior to the phase transformation. Unfortunately, no IPFs were determined at intermediate temperatures, but only after the completed thermal cycle. Thus, it is not possible to ascertain whether reverse reorientation occurred prior to the transformation to austenite. However, any strain recovery due to this reverse reorientation mechanism would be significantly aided by the change in the material's compliance during heating. It has been shown that the Young's modulus for NiTi alloys decreases with temperature reaching a significant minimum at about the start of the reverse transformation followed by a steep increase once the reverse transformation is completed.[44–47] The $Ni_{49.9}Ti_{50.1}$ alloy studied here exhibits similar compliance characteristics that were measured using a dynamic technique[48] and would definitely provide a mechanism for reverse reorientation to occur with increasing temperature.

The initial slopes for the heating curves were also shifted more negatively with increasing applied strain values, which would be due to an increase in twin volume fractions and the internal strain developed in the material (Fig. 5). This also would be consistent with a relaxation or reverse reorientation mechanism discussed above. Moreover, the transformation temperatures A_s and A_f were shifted to higher temperatures with increasing applied strain. This is due to the high internal strain developed during reorientation and twinning of the martensite which resists the phase transformation. However, on cooling, the forward transformation takes place essentially at the same temperature regardless of the applied strain level, and the final room temperature strain recoveries were grouped in two regions, as demonstrated in Fig. 5 and by the step function in recovered thermal strain shown in Fig. 3(a). However, the paths to the strain level at room temperature were very different in all cases. For example, although samples 1(6%) and 2(10%) exhibited the same final recovered strain at room temperature, the paths for getting to that point were significantly different along every portion of the strain-temperature response. This included substantial differences in the initial slope during heating, the magnitude of the TWSME strain between A_s and A_f, and the amount of TWSM strain developed during the forward transformation. Similar differences were observed for the other five samples deformed to higher strain.

Finally, the transient responses during heating show an incomplete transformation to austenite. Neutron diffraction data were acquired at the upper cycle temperature of 200 °C for each sample, which revealed the presence of

untransformed/retained martensite. Through Rietveld refinements, it was estimated that samples 7(22%), 5(18%), and 3(14%) contained ~8%, ~5%, and ~4% volume fraction of retained martensite at 200 °C, even though the stress free A_f temperature for the alloy was 105 °C. No detectable martensite was observed on samples 2(10%) and 1(6%). This retained martensite was mostly of the $(\bar{1}50)_M$, $(010)_M$, and $(230)_M$ orientations that can be both advantageous and disadvantageous to subsequent properties. The retained martensite can affect the internal stress fields aiding the TWSME on cooling, and it can act like "dead" material that does not transform reducing the transforming volume that contributes to the transformation capability of the material.

For a measure of the local internal state, the hkl-specific lattice strains were determined for the critical points noted in Fig. 2, specifically at the maximum applied strain for each case, after unloading to zero stress and after the first thermal cycle. These strains are shown in Fig. 6 and refer to the average strain in a family of variants with common crystallographic orientation (*hkl*) relative to the diffraction vector. They were obtained from the interplanar spacings ($\Delta d_{hkl}/d_{hkl}$) using the single peak fitting method. The $(011)_M$, $(030)_M$, $(\bar{1}20)_M$, and $(\bar{1}21)_M$ lattice strains were selected to represent

the overall general trend observed in the material and are from diffracting lattice planes perpendicular to the loading direction. The dashed lines connecting the lattice strains during loading are not the actual material response since the strains were not continuously monitored but only recorded at the discrete points, i.e., 6%, 10%, 14%, 18%, and 22%.

It is clear from Fig. 6 that internal strains build up with increasing macroscopic applied strain, followed by a decrease after unloading. Yet while the macroscopic far-field stress at this point is 0 MPa after unloading, the internal strains, which are related to the average variant-scale stresses, are still finite and in some cases quite significant, imposing local internal stress concentrations at the variant level. Increasing the temperature (before reaching the A_s) combined with a significant reduction in the material compliance relaxes these constraints and results in further reverse variant reorientation, causing negative slopes in the transient responses as shown in Fig. 5.

Following the first thermal cycle, a further decrease in the internal strains occurs but they are still not fully relaxed, though in some cases are forced into compression, as observed in Fig. 6. Consequently, the starting condition for the TWSME cycling (which are the subsequent thermal
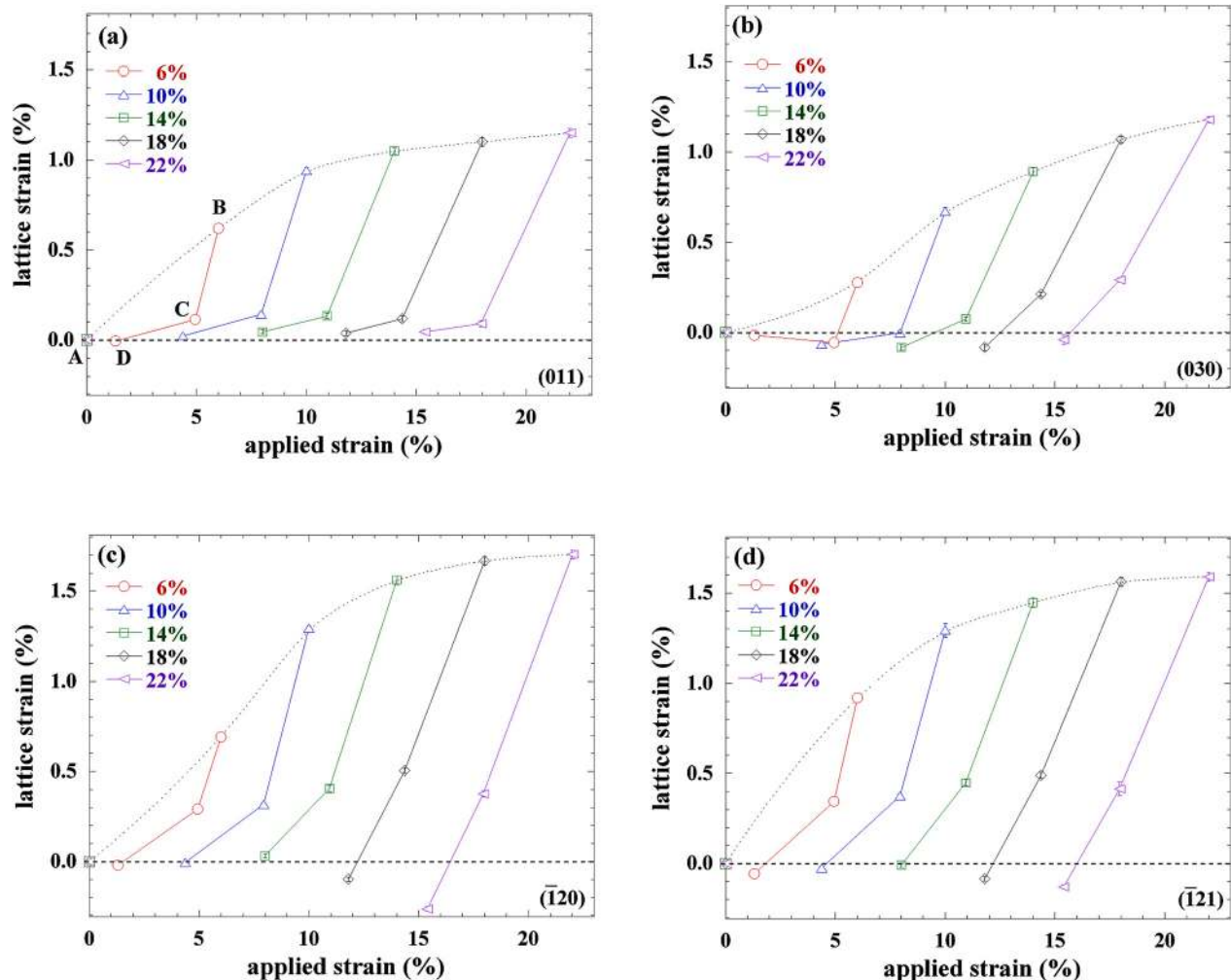

FIG. 6. Lattice strain associated with the (a) $(011)_M$, (b) $(030)_M$, (c) $(\bar{1}20)_M$, and (d) $(\bar{1}21)_M$ planes perpendicular to the loading direction. Lattice strain data at applied strain (B), after unloading (C), and after one thermal cycle (D) are shown for samples loaded between 6% and 22% strain for each of the planes measured.

cycles imposed on the samples) consists of a microstructure that is different from the original microstructure, consisting of some pre-oriented martensite variants, as shown by the IPFs in column D of Fig. 4, stabilized by a small but finite amount of internal stress/strain as defined in Fig. 6.

B. TWSME characterization

The TWSME was introduced in this alloy by a onetime loading in the martensite phase to different applied strain levels. Following this training procedure, the TWSME was characterized by stress-free thermal cycling between room temperature and 200 °C for 10 cycles. The choice of the upper cycle temperature was made to ensure complete transformation when cycling under no-load (after the transient). Figure 7 illustrates the strain-temperature responses of the ensuing TWSME as a function of the applied strain levels.

The first transient heating curves are also included in Fig. 7 as indicated by the dotted lines. It was found that the magnitude of the TWSME strain (calculated as the difference between the cold and hot-shape strains) was maximized in the samples deformed between 14% and 16% strain. This trend is better shown in Fig. 8(a), which is the TWSME strain plotted versus cycle number for each applied strain condition, and in Fig. 8(b) where the TWSME strain is plotted as a function of applied strain level. The TWSME strain started low at 0.5% for sample 1(6%), reached a maximum at 2.2% for sample 4(14%), and dropped to 1.35% for sample 7(22%).

For low applied strains, the deformation was mainly governed by reorientation and detwinning with the preferred selection of the $(\bar{1}50)_M$ and $(010)_M$ orientations as shown in Fig. 4. Most of these orientations (or variants) were reversible upon unloading and thermal cycling, which resulted in a small TWSME as insufficient oriented internal stress fields were generated (Fig. 6) to strongly bias the transformation. At 14% strain, a maximum amount of the easily recoverable $(010)_M$ and $(\bar{1}50)_M$ variants were retained in the microstructure after unloading and even maintained after the first thermal cycle (column D of Fig. 4). In other words, at this
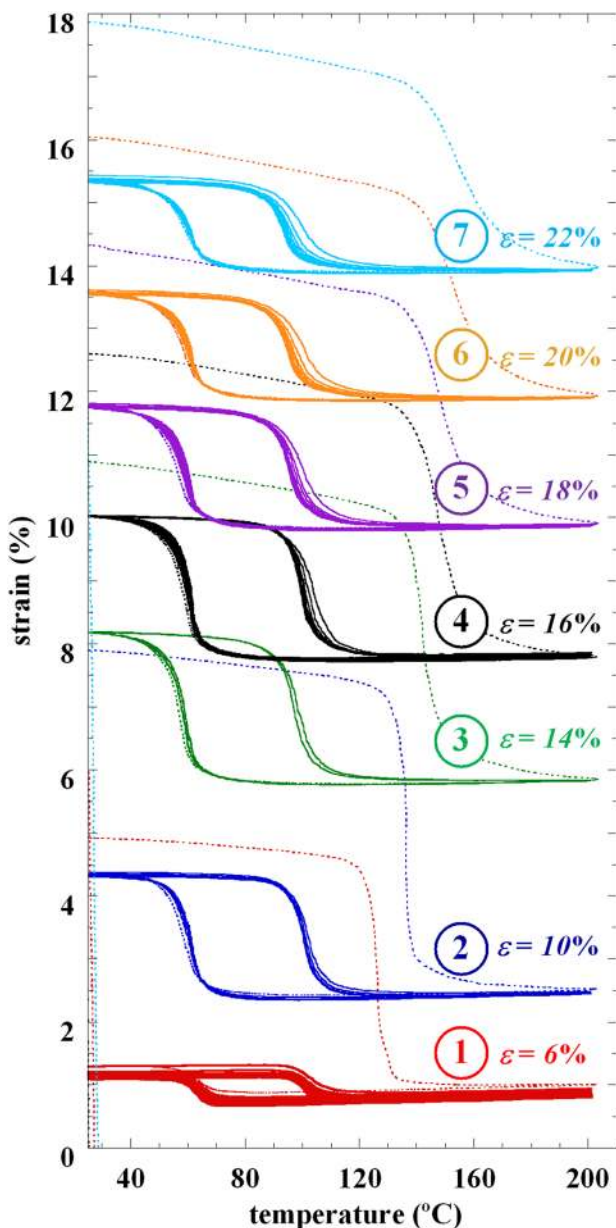

FIG. 7. TWSME strain-temperature responses for all samples strained between 6% and 22%. The transient responses due to the very first heating cycle after unloading are also included (dotted lines).
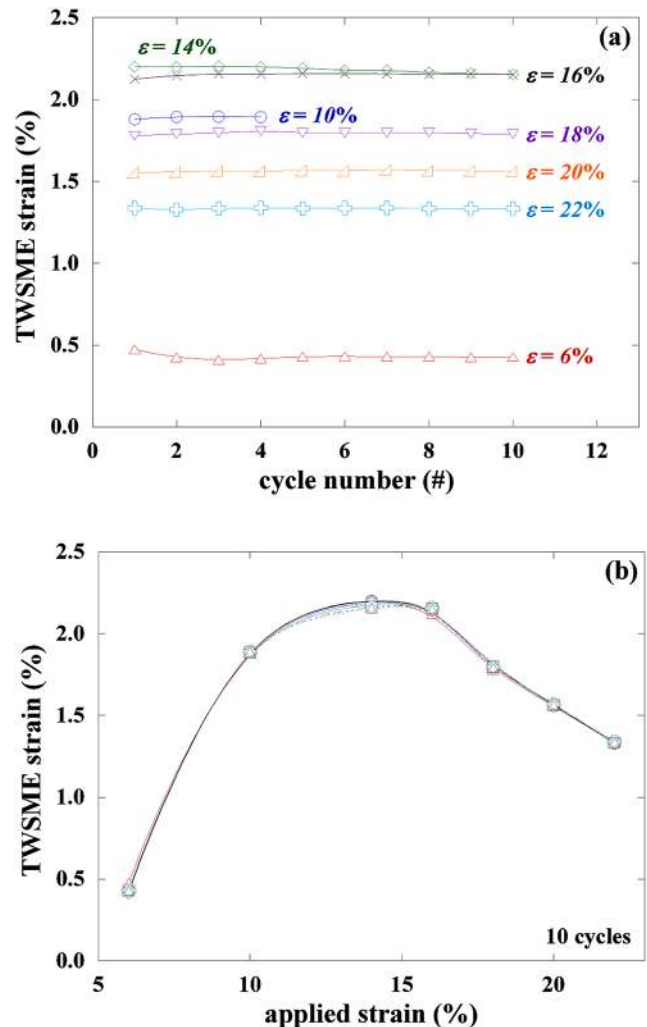

FIG. 8. TWSME strain plotted as a function of (a) cycle number for all strained conditions, and (b) the applied strain level.

applied strain level, a maximum volume fraction of these easily recoverable and high-strain producing variants are now reversibly formed in the microstructure. In addition, the $(20\bar{1})_{B19'}$ twin system was activated at this strain level, but a major portion of these twins were recovered primarily during unloading and also during heating (column D of Fig. 4). Consequently, this applied strain condition maximized the fraction of retained $(010)_M$ and $(\bar{1}50)_M$ variants, while minimizing processes that are more difficult to recover or contribute less strain.

With further straining to higher levels at the second stress plateau (region IV of Fig. 1), less of the easily recoverable $(010)_M$ and $(\bar{1}50)_M$ variants and more of the irreversible twins were retained in the material (column D of Fig. 4), reducing the amount of the transforming volume and strain contributing capability of the material. In addition, over straining can introduce dislocation structures that result in internal strains that do not promote favorable martensite variants and possibly even relax some of the internal constraints that do, resulting in less TWSME. Indirect evidence of this possible slip was presented in the IPFs of Fig. 4 by the grain rotation between the $(010)_M$ and $(230)_M$ orientations (grains that populate the region between these two orientations). A simple change in twinning mechanism alone would show up in the measurements as a discrete shift in texture without gradual rotation.

At every applied strain value, the TWSME strain is shown to be very stable from cycle to cycle (Fig. 8(a)). The stability is also shown in Fig. 8(b) as function of the applied strain that also serves to demonstrate the non-monotonic nature of the TWSME strain behavior. However, it is evident from Fig. 7 that there are some amounts of strain de-evolution (degradation in both the cold and hot-shape strains), particularly in sample 1(6%). As a result, it is appropriate to assess the stability of the TWSME by the strain reduction as a function of cycle count. The strain reductions were calculated from the difference in strain from one cycle to the next measured at room temperature. Compared to the other samples in this study, sample 1(6%) exhibited large
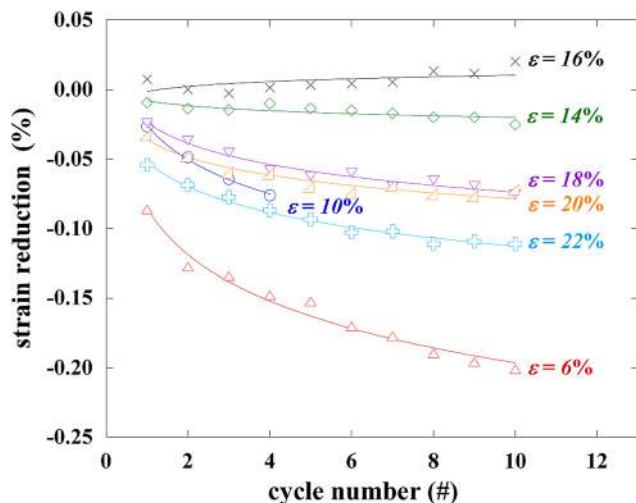
amounts of strain reduction during cycling (Fig. 9) even though the TWSME strain was relatively constant (Fig. 8(a)). Samples 3(14%) and 4(16%) had near perfect dimensional stability as negligible strain reduction was obtained (Fig. 9). At larger applied strains, strain reduction increased again with increasing applied strain values as shown by the samples deformed between 18% and 22% strain. These results indicate that both the magnitude and stability of the TWSME are maximized by the applied strain to 14%-16%. The texture responsible for this optimal behavior includes both maximum contributions from the $(\bar{1}50)/(010)_M$ martensite variants, and minimal contribution, compared to the higher applied strain levels, of $(20\bar{1})_{B19'}$ twins and dislocation induced plasticity in the material. Consequently, this level of applied strain is a balance between maximizing the amount of high-strain, easily recoverable $(\bar{1}50)/(010)_M$ martensite variants that are biased in the material through internal strain and minimizing the amount of less useful $(20\bar{1})_{B19'}$ twinning and plasticity that occurs during the applied strain process.

Other TWSME parameters of importance are the transformation temperatures. The data shown in Fig. 10 illustrate the variation in stability of the transformation temperatures

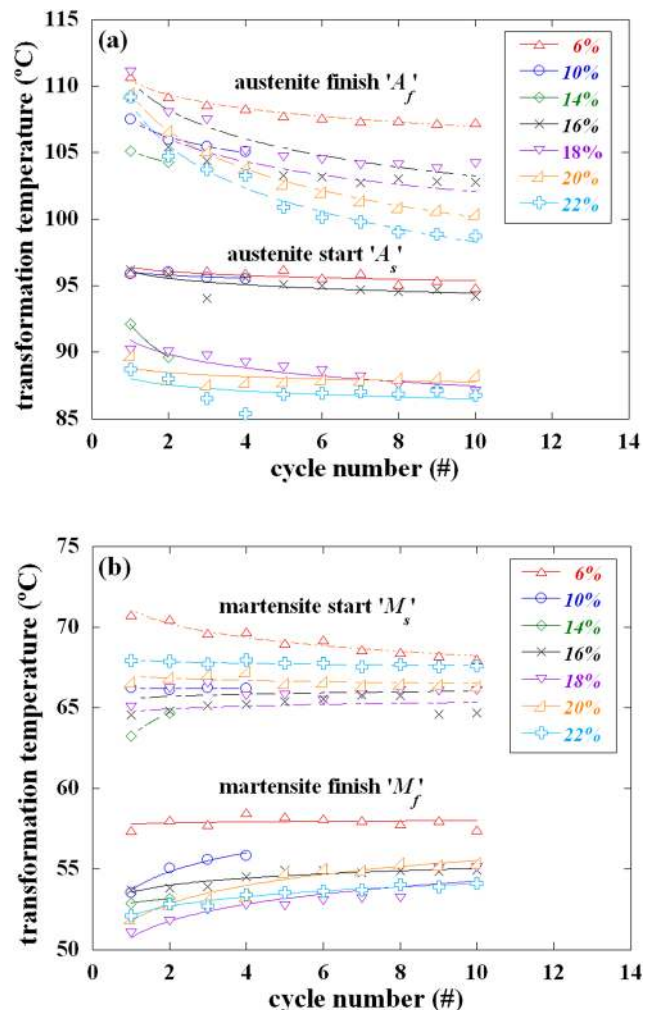FIG. 9. Strain reduction during TWSME thermal cycling (measured at room temperature).

FIG. 10. Transformation temperatures determined during TWSME thermal cycling as a function of increasing cycle number.

with increasing cycle number. For a given applied strain level, the M_s, M_f, and A_s are all shown to be within $2\,^\circ$C during cycling, except for the A_f, which shows larger differences. Keeping in mind that these temperatures were measured using the intercept method, it is reasonable to associate an experimental error of $\pm 2\,^\circ$C to these reported data. Therefore, other than a slight evolution in the A_f temperature with cycling, the transformation temperatures were quite stable regardless of applied strain level. Also, while there were little differences in the transformation temperatures for samples strained between 18% and 22%, there was a general trend. Transformation temperatures were always highest for sample 1(6%) and tended to decrease with increasing applied strain level. However, stability in the transformation temperatures was not an issue when applying this training procedure to Ni$_{49.9}$Ti$_{50.1}$.

IV. SUMMARY

Room-temperature deformation of a martensitic, polycrystalline Ni$_{49.9}$Ti$_{50.1}$ (at. %) shape memory alloy, and its subsequent effect on the TWSME was investigated by combining *ex situ* thermomechanical experiments and *in situ* neutron diffraction measurements. The role of the B19′ martensite deformation on the magnitude and stability of the TWSME was assessed by examining the TWSME transformation strains, strain reduction, and transformation temperatures for a maximum of 10 stress-free thermal cycles. The following conclusions are reached.

1. The nature of the room-temperature stress-strain response was correlated with the texture evolution observed at each selected applied strain value.
   a. Deformation to 6% strain, which corresponds to the end of region II deformation behavior (Fig. 1), was mainly dominated by easy martensite reorientation and detwinning with preferred selection of the $(\bar{1}50)_M$ and $(010)_M$ orientations along the loading direction, most of which were easily recovered after thermal cycling.
   b. From 6% to 12% strain (region III in Fig. 1), deformation was still primarily accommodated by martensite reorientation and detwinning, but a secondary deformation mechanism was also observed that produced a strong reflection at the $(230)_M$ pole. This secondary mechanism was related to the $(20\bar{1})_{B19'}$ twin system. While the majority of this twin system was irreversible, fractions were also recovered after thermal cycling.
   c. Further deformation resulted in a significant change in work hardening (and a transition into region IV). In this region, at strains from 14% to 22%, no new texture components were observed, but deformation seemed to be dominated by processes that were additionally irreversible in nature. More of the $(20\bar{1})_{B19'}$ twins were retained in the sample after deformation and thermal cycling. Also, indirect evidence of slip mechanisms was also captured by the slight rotation of poles (e.g., $(010)_M$) during deformation.
2. In general, reversible strains were attributed to the elastic recovery and reverse reorientation during unloading, additional reverse orientation, and recovery of $(\bar{1}50)_M$ and $(010)_M$ martensite variants during thermal cycling and partial reversibility of the $(20\bar{1})_{B19'}$ twins. Irreversible strains were attributed to the permanent deformation twins and dislocations structures that cause a loss of correspondence to the original parent phase. Irreversible strains exceeded the reversible strains above $\sim$12% applied strain (region IV) as the deformation twins and dislocation processes started to dominate the behavior.
3. Training via martensite deformation was shown to be a quick and effective way to introduce stable TWSME.
4. The applied strain levels dictated the magnitude and stability of the ensuing TWSME. Straining to 14%-16%, or to the end of region III, was found to be optimum for this material under the current testing conditions. Deformation to these strains maximized the amount of biased $(\bar{1}50)_M$ and $(010)_M$ martensite variants present in the material, while compared to higher strain levels, minimized the amount of $(20\bar{1})_{B19'}$ twinning. Under these conditions, a stable TWSME strain of 2.2% was obtained with near-zero strain reduction. These strain calculations (transformation and reduction) in addition to the transformation temperature data are relevant to the design of shape memory alloy actuators that employ the two-way effect.
5. Further work is needed to assess the consequences of changing one or more of the test conditions (tension/compression, strain/stress control, loading/heating rates, and the upper/lower cycle temperatures) that may result in different behaviors. Moreover the transient response was not fully explored at this point, and more work is needed to explain this behavior.

[1]K. Yamauchi, I. Ohkata, K. Tsuchiya, and S. Miyazaki, *Shape Memory and Superelastic Alloys: Technologies and Applications* (Woodhead, 2011).
[2]D. S. Grummon, JOM **55**, 24 (2003).
[3]X. M. Zhang, J. Fernandez, and J. M. Guilemany, Mater. Sci. Eng., A **438–440**, 431 (2006).
[4]R. Lahoz and J. A. Puertolas, J. Alloys Compd. **381**, 130 (2004).
[5]Y. Liu and P. G. McCormick, Acta Metall. Mater. **38**, 1321 (1990).
[6]H. Scherngell and A. C. Kneissl, Scr. Mater. **39**, 205 (1998).
[7]K. C. Atli, I. Karaman, R.D. Noebe, and D. Gaydosh, "The Effect of Training on Two-Way Shape Memory Effect of Binary NiTi and NiTi Based Ternary High Temperature Shape Memory Alloys," Mater. Sci. Eng., A. Available at: http://dx.doi.org/10.1016/j.msea.2012.10.009.
[8]K. C. Atli, I. Karaman, and R. D. Noebe, Scr. Mater. **65**, 903 (2011).

[9]L. Contardo and G. Guenin, Acta Metall. Mater. **38**, 1267 (1990).

[10]R. Stalmans, J. Van Humbeeck, and L. Delaey, Acta Metall. Mater. **40**, 501 (1992).

[11]L. Wang, X. Meng, W. Cai, and L. Zhao, J. Mater. Sci. Technol. **17**, 13 (2001).

[12]D. A. Hebda and S. R. White, Smart Mater. Struct. **4**, 298 (1995).

[13]Y. Liu, Y. Liu, and J. Van Humbeeck, Acta Mater. **47**, 199 (1998).

[14]K. Wada and Y. Liu, J. Alloys Compd. **449**, 125 (2008).

[15]Y. I. Yoo and J. J. Lee, Phys. Procedia **22**, 449 (2011).

[16]R. Lahoz, L. Gracia-Villa, and J. A. Puertolas, J. Eng. Mater. Technol. **124**, 397 (2002).

[17]X. L. Meng, W. Cai, Y. F. Zheng, Y. B. Rao, and L. C. Zhao, Mater. Lett. **57**, 4206 (2003).

[18]X. L. Meng, Y. F. Zheng, W. Cai, and L. C. Zhao, J. Alloys Compd. **372**, 180 (2004).

[19]Z. Balak and S. M. Abbasi, Mater. Des. **32**, 3992 (2011).

[20]J. Perkins and R. Sponholz, Metall. Mater. Trans. A **15**, 313 (1984).

[21]S. Eucken and T. W. Duerig, Acta Metall. **37**, 2245 (1989).

[22]J. M. Guilemany, B. G. Mellor, and J. Fernandez, Mater. Lett. **13**, 105 (1992).

[23]M. Nishida and T. Honma, Scr. Metall. **18**, 1293 (1984).

[24]C.-Y. Chang, D. Vokoun, and C.-T. Hu, Metall. Mater. Trans. A **32**, 1629 (2001).

[25]J. Pons, M. Sade, F. C. Lovey, and E. Cesari, Mater. Trans., JIM **34**, 888 (1993).

[26]M. S. Shakeri, J. Khalil-Allafi, V. Abbasi-Chianeh, and A. Ghabchi, J. Alloys Compd. **485**, 320 (2009).

[27]K. Otsuka and X. Ren, Mater. Sci. Eng., A **312**, 207 (2001).

[28]S. Qiu, B. Clausen, S. A. Padula II, R. D. Noebe, and R. Vaidyanathan, Acta Mater. **59**, 5055 (2011).

[29]K. Madangopal and R. Banerjee, Scr. Metall. Mater. **27**, 1627 (1992).

[30]J. X. Zhang, M. Sato, and A. Ishida, Acta Mater. **54**, 1185 (2006).

[31]T. Ezaz, H. Sehitoglu, and H. J. Maier, Acta Mater. **59**, 5893 (2011).

[32]Z. Xie, Y. Liu, and J. Van Humbeeck, Acta Mater. **46**, 1989 (1998).

[33]Y. Liu, Z. Xie, J. Van Humbeeck, and L. Delaey, Acta Mater. **46**, 4325 (1998).

[34]M. Nishida, S. Ii, K. Kitamura, T. Furukawa, A. Chiba, T. Hara, and K. Hiraga, Scr. Mater. **39**, 1749 (1998).

[35]O. Benafan, Ph.D. dissertation, University of Central Florida, Orlando, 2012.

[36]S. Manchiraju, D. Gaydosh, O. Benafan, R. Noebe, R. Vaidyanathan, and P. M. Anderson, Acta Mater. **59**, 5238 (2011).

[37]S. Qiu, V. B. Krishnan, S. A. Padula II, R. D. Noebe, D. W. Brown, B. Clausen, and R. Vaidyanathan, Appl. Phys. Lett. **95**, 141906 (2009).

[38]S. A. Padula II, S. Qiu, D. J. Gaydosh, R. D. Noebe, G. S. Bigelow, A. Garg, and R. Vaidyanathan, Metall. Mater. Trans. A **43**, 4610 (2012).

[39]M. A. M. Bourke, D. C. Dunand, and E. Ustundag, Appl. Phys. A **74**, s1707 (2002).

[40]H. Rietveld, J. Appl. Crystallogr. **2**, 65 (1969).

[41]A. C. Larson and R. B. Von Dreele, *General Structure Analysis System (GSAS)*, Los Alamos National Laboratory, Report No. LAUR 86-748, 2004.

[42]R. B. Von Dreele, J. Appl. Crystallogr. **30**, 517 (1997).

[43]A. P. Stebner, Ph.D. dissertation, Northwestern University, Evanston, 2012.

[44]A. Stebner, S. Padula, R. Noebe, B. Lerch, and D. Quinn, J. Intell. Mater. Syst. Struct. **20**, 2107 (2009).

[45]X. Ren and K. Otsuka, Scr. Mater. **38**, 1669 (1998).

[46]T. M. Brill, S. Mittelbach, W. Assmus, M. Mullner, and B. Luthi, J. Phys.: Condens. Matter. **3**, 9621 (1991).

[47]X. Huang, G. J. Ackland, and K. M. Rabe, Nature Mater. **2**, 307 (2003).

[48]O. Benafan, R. D. Noebe, S. A. Padula II, B. A. Lerch, D. J. Gaydosh, A. Garg, G. S. Bigelow, K. An, and R. Vaidyanathan, "Temperature dependent behavior of a polycrystalline NiTi shape memory alloy around the transformation regime" (unpublished).